

Obtaining diffraction patterns from annular dark-field STEM-in-SEM images: Towards a better understanding of image contrast



Jason Holm*, Benjamin Caplins, Jason Killgore

National Institute of Standards and Technology, Boulder, CO 80305, United States

ARTICLE INFO

Keywords:

STEM-in-SEM
Diffraction pattern
Scattering intensity
Aperture
Image contrast
Contrast reversal
Contrast inversion
Annular dark field

ABSTRACT

This contribution demonstrates experimentally how a series of annular dark-field transmission images collected in a scanning electron microscope (SEM) with a basic solid-state detector can be used to quantify electron scattering distributions (i.e., diffraction patterns). The technique is demonstrated at different primary electron energies with a polycrystalline aluminum sample and two amorphous samples comprising vastly different mass-thicknesses. Contrast reversal is demonstrated in both amorphous samples, suggesting that intuitive image contrast interpretation is not always straightforward even for ultrathin, low atomic number samples. We briefly address how the scattering distributions obtained here can be used as an aid to interpret contrast in annular dark-field images, and how to set up imaging conditions to obtain intuitively interpretable contrast from samples with regions of significantly different thickness.

1. Introduction

Scanning electron microscopes (SEMs) are ubiquitous in materials analysis labs because the focused electron probe can provide useful information about diverse samples on different length scales. Detectors designed to collect many signals (e.g., secondary electrons, back-scattered electrons, X-rays, photons, etc.) are widely available and sufficiently well-developed that non-specialists can quickly obtain meaningful information. Transmission electron detectors are also widely available for imaging electron-transparent samples. Although advances have been made to better utilize the transmitted electron signal quantitatively [1–3], part of the reason it has not been more diligently pursued is that samples must be extremely thin. Otherwise, plural- and multiple-scattering can make contrast in transmission images challenging to interpret [4–8].

In conventional scanning transmission electron microscopy (STEM) and conventional transmission electron microscopy (TEM), it is customary to collect an image and one or more diffraction patterns to be used as an aid to understand image contrast, to set up different imaging modes, and to obtain quantitative information about the sample [9]. One of the challenges with interpreting STEM-in-SEM image contrast is that detectors capable of collecting on-axis transmission diffraction patterns are not widely available. To that end, this contribution

addresses two needs of the STEM-in-SEM community. First, it demonstrates experimentally in an SEM how a series of images collected with a basic solid-state diode detector can be used to quantify electron scattering distributions (i.e., diffraction patterns) of amorphous and polycrystalline samples. Second, because annular dark-field (ADF) image contrast is strongly affected by beam energy, detector geometry, and specimen thickness [6,10–12], we consider two amorphous samples at different imaging conditions, and briefly describe caveats involved with interpreting STEM-in-SEM ADF image contrast. We show that ADF contrast reversal can happen even for ultrathin, low atomic number samples, and address how to set up imaging conditions to obtain intuitively interpretable contrast from samples with regions of vastly different mass-thickness.

2. Experimental

A Zeiss Auriga SEM¹ was used at 5 keV to deposit amorphous pads of different thickness and composition on ultrathin carbon support films (Ted Pella, Prod. No. 01824). Two different precursors were used: C₁₀H₈ (phenanthrene) was used to deposit ultrathin carbon pads, and C₉H₁₆Pt (methylcyclopentadienyl(trimethyl)platinum-IV) was used to deposit thicker pads. Although the pads deposited from C₉H₁₆Pt are a mixture of hydrogen, carbon, and platinum, they will be referred to

Contribution of NIST, not subject to copyright in the United States. This research did not receive any specific grant from funding agencies in the public, commercial, or not-for-profit sectors.

* Corresponding author.

E-mail address: jason.holm@nist.gov (J. Holm).

¹ Any mention of commercial products is for information only, it does not imply recommendation or endorsement by NIST.

hereafter as platinum pads. Pad thicknesses were controlled by increasing the number of times the electron beam was scanned over each pad. For example, the beam was scanned once over the area corresponding to pad 1, twice over pad 2, three times over pad 3, and so on, up to nine times over pad 9 for the carbon sample. For the platinum sample pads, a uniformly thin platinum substrate was first deposited (40 scans) on the ultrathin carbon support film, and nine discrete platinum pads were then deposited on top of the platinum substrate. Platinum pad 1 was scanned 25 times, pad 2 was scanned 50 times, pad 3 was scanned 75 times, and so on, up to 225 scans for pad 9. The carbon and platinum pads were deposited near pre-existing holes in the ultrathin carbon film so that STEM detector gain settings could be adjusted to obtain non-zero, quantifiable background vacuum intensities. Using identical deposition settings, carbon and platinum pads were also deposited on a flat piece of Si wafer, and an atomic force microscope (AFM) was used to measure the pad thicknesses. A polycrystalline aluminum sample (Ted Pella, Prod. No. 619, thickness ≈ 30 nm) was used without modification.

Samples were imaged in ADF transmission mode using a Zeiss LEO 1525 SEM and a KE Developments STEM detector equipped with a modular aperture system [8]. Fig. 1a shows a schematic of the experimental setup with parameters including camera length, CL , inner and outer aperture radii, R_i and R_o , inner and outer STEM detector acceptance angles, β_i and β_o , the midpoint of the inner and outer detector acceptance angles, β_{mid} , and the beam convergence angle, α . A mask with an annular aperture having $R_i \approx 0.205$ mm and $R_o \approx 0.214$ mm (Fig. 1b, inset image) was placed over one of the STEM detector diodes, and the aperture was centered on the optic axis using the STEM detector xyz-positioning stage. Camera length was determined as follows: With the sample removed from the field of view, the working distance of a well-focused image of the top of the STEM detector mask was established. The sample was then brought into the field of view and positioned immediately above the mask. A well-focused image of the sample was recorded, and both the working distance and the sample stage z-position were noted. The difference in working distances between the two images provided an initial value for the camera length, and all successive camera length changes were implemented by moving the sample stage in the z-direction. The sample stage z-position indicated by the SEM software is adequate to illustrate the technique outlined here without calibration, but it can be calibrated using a traceable standard. The working distance of successive images could also be used to determine camera length, but those values will depend on the ability of the user to consistently establish well-focused images and cannot be easily calibrated.

Fig. 1b summarizes the acceptance angle range and span (span = $d\beta = \beta_o - \beta_i$) as a function of CL for the annular aperture. For example, when $CL = 3.6$ mm, $\beta_i \approx 57$ mrad and $\beta_o \approx 59$ mrad. Note that $d\beta$ decreases with increasing CL , meaning that intensity distributions as measured here are effectively skewed to greater angles because

the signal is collected over a wider span when the sample is closer to the detector. Also, because focus is kept at the sample as the CL is changed, α becomes more convergent as the sample approaches the pole piece (Fig. 1b, pink curve). Although α only changes by a few mrad over the experimental conditions used here, this observation is important for rigorous quantitative analyses because the scattering pattern will broaden as α increases. A $20 \mu\text{m}$ diameter primary electron beam limiting aperture was used for imaging the aluminum and platinum pads; a $30 \mu\text{m}$ aperture was used for the carbon pads. With these apertures, beam convergence angle ranges calculated based on a factory-supplied equation were approximately $1.6 \text{ mrad} < \alpha < 2.2 \text{ mrad}$ for the aluminum sample, $1.6 \text{ mrad} < \alpha < 3.8 \text{ mrad}$ for the platinum sample, and $2.9 \text{ mrad} < \alpha < 8.4 \text{ mrad}$ for the carbon sample. These calculated ranges match well with experimental measurements on the same SEM [13]. Samples were positioned between the pole piece and the STEM detector using a cantilever style holder attached to the SEM sample positioning stage [8].

For each of the three samples, the STEM detector amplifier dc offset was adjusted to obtain quantifiable background vacuum image intensities at the through-holes in the ultrathin carbon substrate (i.e., minimum grey level greater than zero), and the gain was adjusted to keep the sample signal from saturating the detector (i.e., maximum grey level less than 255). With the STEM detector held stationary and amplifier settings held constant, each sample was stepped from a short CL (i.e., with the sample positioned near the masked detector) towards the pole piece in small increments. For example, the step increment was 0.1 mm for the aluminum sample. At each step, an 8-bit ADF STEM image was recorded. Three image sets of the carbon sample (i.e., at 10 keV, 20 keV, and 30 keV), one of the platinum sample (30 keV), and one of the aluminum sample (30 keV) were recorded this way. In each image, the average sample intensity (I_{avg}) and its standard deviation (SD), and the background vacuum intensity (I_{bgd}) were measured within specified regions (i.e., within the dashed rectangles shown in Fig. 2) using ImageJ software. Intensity measurements from each image set were combined into intensity distributions as a function of β_{mid} (Fig. 3a).

3. Results

Fig. 2 shows two cropped, but otherwise unmodified ADF transmission images of the aluminum sample. The image collected at $\beta_{mid} \approx 48.1$ mrad (Fig. 2a) shows widespread speckle suggestive of polycrystallinity with $I_{avg} = 54.5$, and the image collected at $\beta_{mid} \approx 65.3$ mrad (Fig. 2b) shows minimal speckle with $I_{avg} = 37.5$. Fig. 3a shows the average intensity, the standard deviation, and the background vacuum intensity distributions measured from the entire aluminum image set. Points included on the standard deviation curve indicate β_{mid} for the sampling/imaging interval (i.e., one image was collected at each point). Both distributions exhibit distinct peaks that align closely with

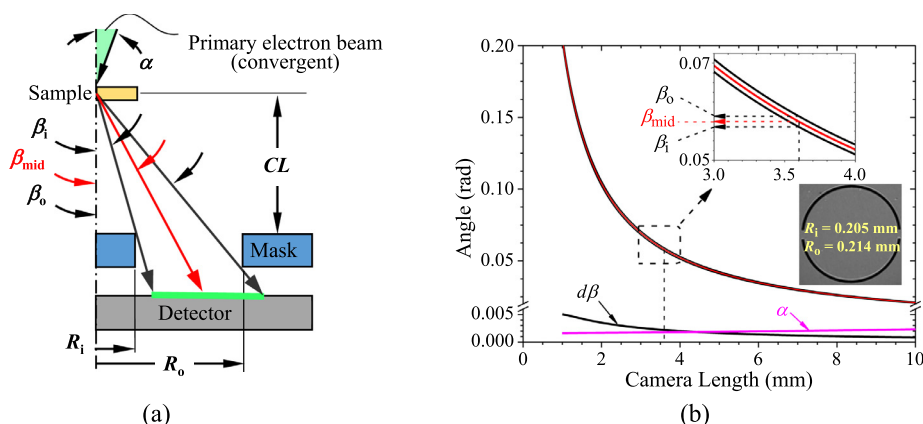


Fig. 1. (a) A schematic of the relationship between camera length, CL , and effective STEM detector acceptance half-angles, β , for an annular aperture with inner and outer radii, R_i and R_o . The beam convergence angle is α . (b) STEM detector acceptance half-angles and span $d\beta = \beta_o - \beta_i$ calculated as a function of CL for the aperture shown in the inset image. The region between the black lines encompasses the acceptance angles for an aperture with $R_i \approx 0.205$ mm and $R_o \approx 0.214$ mm. The red line indicates β_{mid} , the midpoint between β_i and β_o . The beam convergence angle, α , is shown in pink for the $20 \mu\text{m}$ diameter primary electron beam aperture with the aluminum sample. (For interpretation of the references to color in this figure legend, the reader is referred to the web version of this article.)

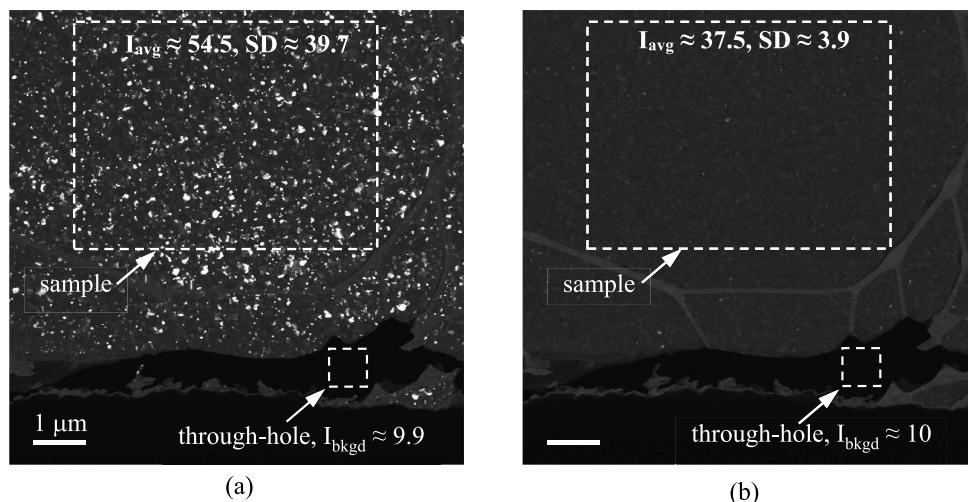


Fig. 2. ADF images of the polycrystalline aluminum sample showing regions in which the average intensity (I_{avg}), the standard deviation (SD), and the background vacuum intensity (I_{bkgd}) were recorded. Images were collected at (a) $\beta_{mid} \approx 48.1$ mrad ($d\beta \approx 1.9$ mrad, $\alpha \approx 1.8$ mrad), and at (b) $\beta_{mid} \approx 65.3$ mrad ($d\beta \approx 2.4$ mrad, $\alpha \approx 1.8$ mrad).

Bragg reflections calculated for aluminum at 30 keV. For example, the peaks near 29 mrad and 48 mrad can be tentatively associated with (111) and (220) reflections, respectively.

Because the acceptance angle span $d\beta$ increases with decreasing CL (Fig. 1b), the raw intensity distributions are effectively skewed towards greater scattering angles [14]. To account for the variation in $d\beta$ and for the non-zero background vacuum intensity, in each image the measured background vacuum intensity was subtracted from the corresponding sample intensity measurement and the difference was divided by $d\beta$ specific to that image. The result for the aluminum sample is shown in Fig. 3b along with the standard deviation divided by $d\beta$. After processing, an exponentially decreasing background can be observed in the aluminum intensity distribution.

Average thicknesses of the carbon and platinum pads measured by AFM are summarized in Fig. 4. Both samples exhibited a linear relationship between pad thickness and deposition conditions. The average thickness was $1.0 \text{ nm} \pm 0.1 \text{ nm}$ for carbon pad 1, and $9.2 \text{ nm} \pm 0.2 \text{ nm}$ for carbon pad 9. The platinum substrate was $35.5 \text{ nm} \pm 1.0 \text{ nm}$ thick, and the average thickness of platinum pads 1 and 9, measured from the silicon surface to the top of the pads, were $73.0 \text{ nm} \pm 1.4 \text{ nm}$ and $316.8 \text{ nm} \pm 1.6 \text{ nm}$, respectively. The inset height profile maps visually demonstrate that individual pads are uniformly thick over the range where image intensities were measured.

Fig. 5 shows ADF transmission images of the carbon pads. Images in the top row (Fig. 5a) were recorded at 10 keV, and images in the bottom row (Fig. 5b) at 30 keV. Acceptance angles ($\beta_i < \beta < \beta_o$) and the corresponding beam convergence angle (α) are indicated under their respective images. Inset dashed squares in Fig. 5b are representative of the regions over which intensities were measured in each image, and

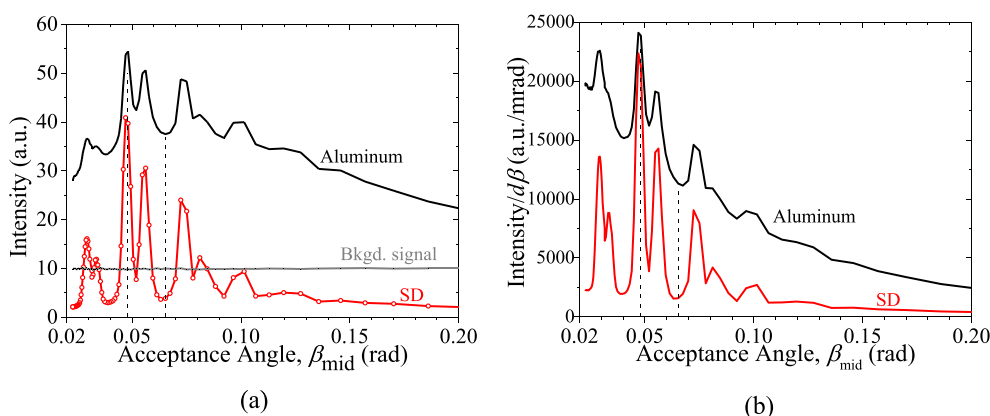


Fig. 3. Intensity and standard deviation distributions of the polycrystalline aluminum sample image set. Two vertical dashed lines indicate β_{mid} at which the images in Fig. 2 were recorded. (a) Raw image intensity data. Points on the standard deviation curve indicate β_{mid} at which each image was recorded. The background signal corresponds to the vacuum intensity measurement at the through-hole. (b) Intensity data corrected for non-zero background vacuum level and normalized to $d\beta$, and SD normalized to $d\beta$.

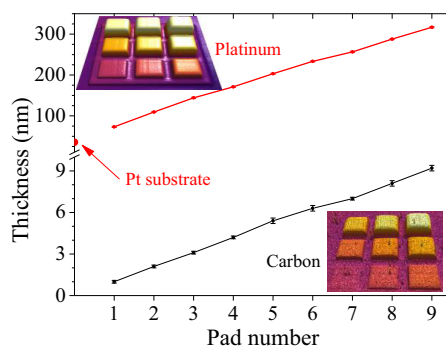


Fig. 4. Carbon (black curve) and platinum (red curve) pad thickness measurements using AFM. The y-axis represents average thickness measured from the silicon substrate to the top of the deposited pad, with error bars shown at each point. Inset AFM height maps demonstrate uniform thickness over the regions where image intensities were measured. Pads are approximately $1.0 \mu\text{m}$ squares. (For interpretation of the references to color in this figure legend, the reader is referred to the web version of this article.)

inset numbers indicate increasing pad thickness: 1 is thinnest, 9 is thickest. Although STEM detector amplifier settings were unchanged for all three carbon image sets, the 10 keV images in Fig. 5a were post-processed so that contrast could be observed by eye. For example, the image intensity histogram was rescaled so that intensities between 31 and 42 spanned the 8-bit grayscale range. Images in Fig. 5b were cropped but otherwise unmodified.

Contrast reversal can be observed at 10 keV: the left image in Fig. 5a exhibits bright-field character, the middle image exhibits no useful

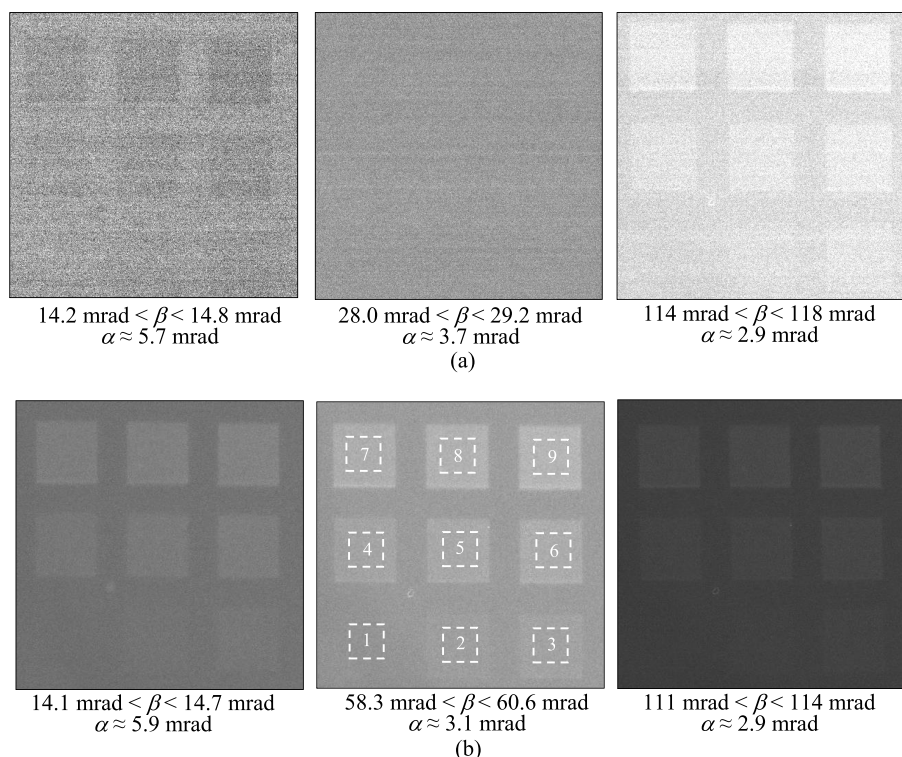


Fig. 5. ADF images of the carbon sample recorded at (a) 10 keV and (b) 30 keV. Acceptance angle ranges ($\beta_i < \beta < \beta_o$) and beam convergence angles are shown under their corresponding images. Inset numbers indicate increasing pad thicknesses (1 = thinnest, 9 = thickest), and dashed squares indicate representative areas over which pad intensities were measured. Pads are $\sim 1.0 \mu\text{m}$ on each side. STEM detector gain and dc offset were constant for all images, but the images in (a) were adjusted so that contrast could be observed by eye. (Details are described in text.)

contrast, and the right image exhibits dark-field character. At 20 keV (not shown) and 30 keV (Fig. 5b) the images all exhibit dark-field character (i.e., the thinnest pad is darkest, and the thickest pad is brightest), and no contrast reversal is observed over the acceptance angle range used here.

Intensity distributions of the carbon sample are shown in Fig. 6a. Distributions corrected for non-zero background vacuum intensity and

$d\beta$ are shown in Fig. 6b. For clarity, only the curves for the background vacuum, the carbon substrate, and pads 1, 5, and 9 are shown. Three vertical dashed lines indicate β_{mid} at which the images in Fig. 5 were collected, and points included on different curves indicate the sampling/imaging interval (i.e., one image was collected at each point.) Since all carbon images were collected at the same detector amplifier setting, distributions in Fig. 6b were also normalized to the primary

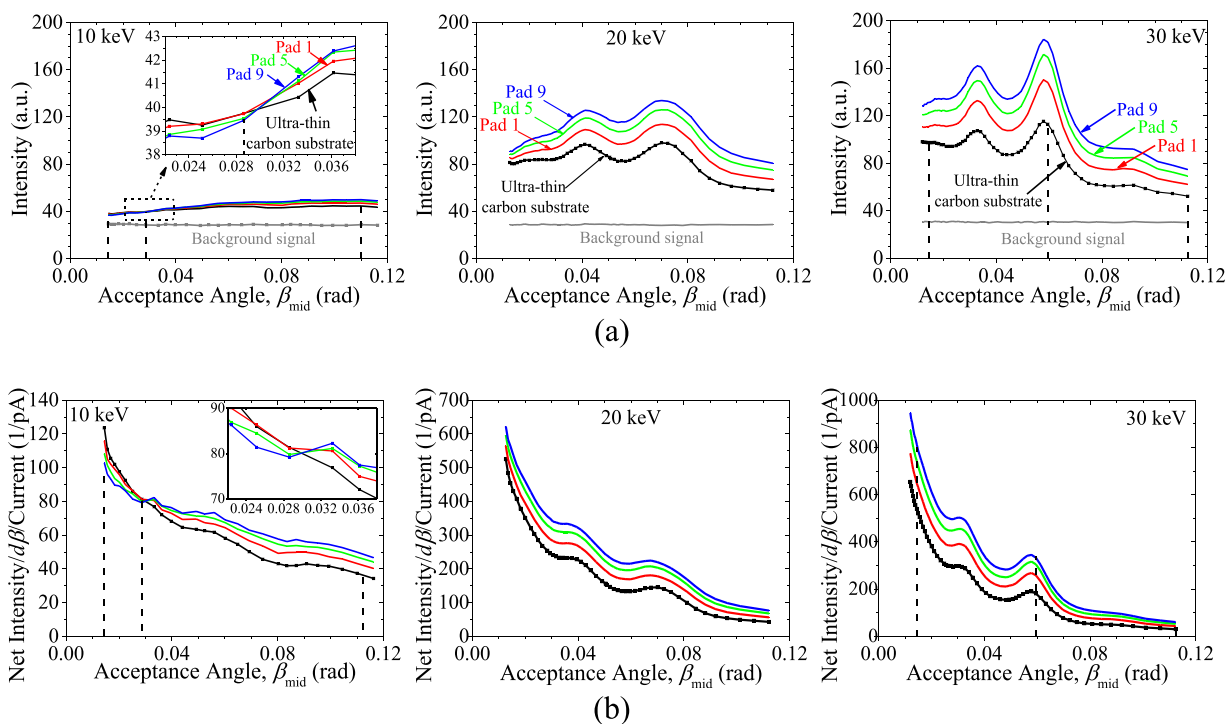


Fig. 6. Image intensity distributions of the carbon sample at 10 keV, 20 keV, and 30 keV. (a) Unmodified distributions. (b) Distributions corrected for $d\beta$, non-zero background intensity, and normalized to primary electron beam current. Vertical dashed lines indicate β_{mid} at which the images in Fig. 5 were recorded, and points indicate β_{mid} for images.

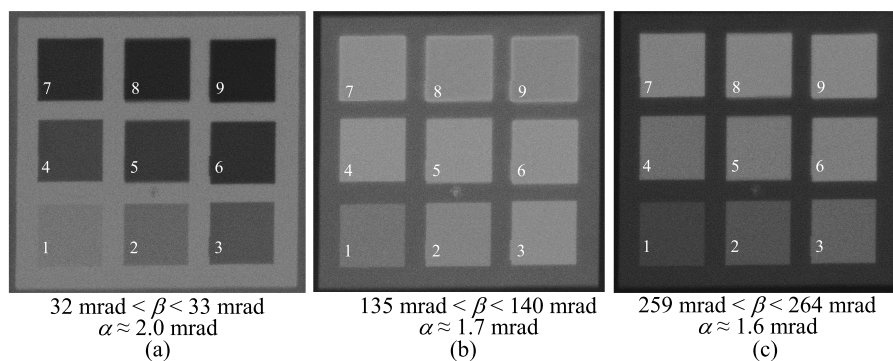


Fig. 7. ADF images of the platinum sample for (a) $\beta_{\text{mid}} \approx 32.5$ mrad, (b) $\beta_{\text{mid}} \approx 137.5$ mrad, and (c) $\beta_{\text{mid}} \approx 261.5$ mrad. The edge of the platinum substrate and the ultrathin carbon support film are visible around the perimeter of each image. Pads are $1.0 \mu\text{m}$ on each side.

electron beam current which was measured using a Faraday cup at 10, 20, and 30 keV with the sample removed from the optic axis. Note that normalization to the primary electron beam current is only intended to provide an approximate visual indication of the relative signal strengths. Image intensity will also depend on electron energy at the detector, which will vary with primary electron energy and losses due to scattering.

All distributions of the carbon sample (Fig. 6) show two broad peaks that generally exhibit increasing intensity with increasing sample thickness. The peaks also become narrower and shift to smaller angles with increasing primary electron energy because the scattering cross-section decreases with increasing electron energy. Unlike the 20 keV and 30 keV distributions which do not intersect at any of the experimental conditions, the 10 keV distributions all intersect at $\beta_{\text{mid}} \approx 30$ mrad where no image contrast is observed (Fig. 5a, middle image). This acceptance angle coincides with the conditions where the images change character from bright-field to dark-field.

Fig. 7 shows ADF images of the platinum sample recorded at different β_{mid} . Pad thicknesses increase with inset number (i.e., pad 1 is thinnest, 9 is thickest), and contrast reversal is evident. In Fig. 7a, pad intensities vary inversely with thickness: the thinnest pad exhibits the maximum intensity, the thickest pad exhibits the minimum intensity. In Fig. 7b, intensities do not vary directly with thickness: pads 1 and 9 are darker than the others. In Fig. 7c, pad intensities increase with sample thickness: the minimum intensity is exhibited by the thinnest pad, and the maximum intensity by the thickest pad. Note that the platinum substrate is the thinnest region of the electron beam-deposited platinum sample, and the observed substrate intensities follow the trends observed in each image of Fig. 7.

Fig. 8a shows raw intensity distributions of the platinum sample, and Fig. 8b shows distributions corrected for non-zero background vacuum intensity and $d\beta$. Distributions for the platinum substrate, the

ultrathin carbon support film, and the background vacuum intensity are also included. Points comprising intensity data from pad 9 are shown to demonstrate the sampling/imaging interval, and three vertical dashed lines indicate β_{mid} at which the images in Fig. 7 were recorded.

The ultrathin carbon substrate distributions in Fig. 8 exhibit two distinct peaks and are essentially identical to the 30 keV distributions shown for the carbon sample in Fig. 6, demonstrating repeatability of the technique. Distributions of the platinum substrate and the thinnest platinum pads also exhibit two peaks like the ultrathin carbon substrate, but with different intensities. With increasing pad thickness, the platinum distributions broaden significantly until only one broad peak can be observed.

4. Discussion

4.1. Quantifying intensity distributions

Assuming detector efficiency doesn't change significantly with the scattering angles and electron energy (i.e., the detector response may be different at 10 keV than at 30 keV, but it does not vary significantly within a few hundred eV of the primary electron energy setpoint), ADF image intensity should be proportional to the number of detected electrons. Therefore, intensity distributions derived from a series of images, where each image is collected at a different acceptance angle and with a narrow acceptance angle span, should closely replicate the transmitted electron scattering distribution (i.e., the diffraction pattern) [14]. For comparison with a diffraction pattern collected in a more conventional manner, the inset image of Fig. 9 shows a 30 keV diffraction pattern of the polycrystalline aluminum sample recorded using a pixelated STEM detector on the same SEM [13]. The azimuthally-integrated radial intensity profile obtained from the inset image is plotted in black on the lower x-axis in pixel coordinates.

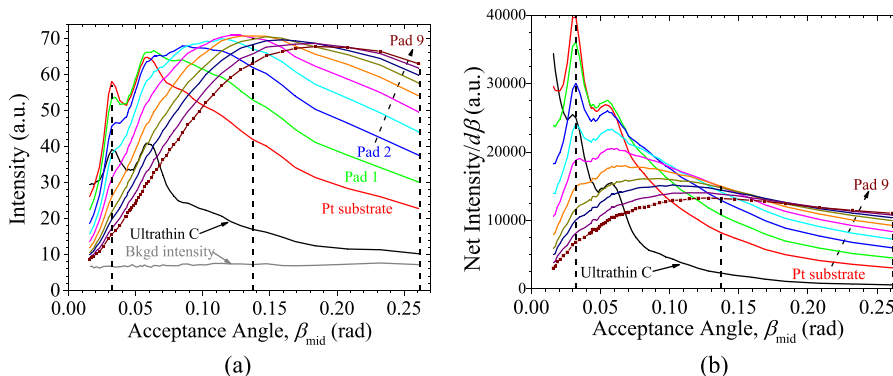


Fig. 8. Intensity distributions of the platinum sample at 30 keV. (a) Uncorrected data, and (b) data corrected for non-zero background intensity and $d\beta$. Points indicate β_{mid} at which images were recorded, vertical dashed lines indicate the angles at which the images in Fig. 7 were recorded.

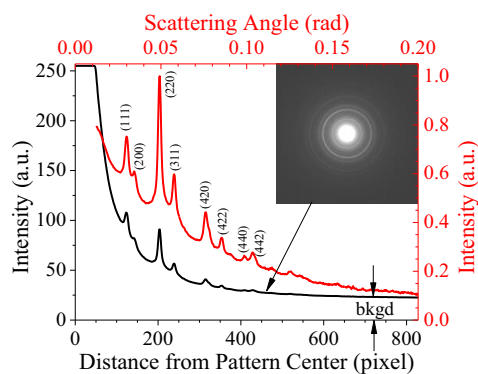


Fig. 9. A polycrystalline aluminum diffraction pattern obtained with a pixelated STEM detector and two associated radial intensity profiles. The inset image was obtained at $CL \approx 11.3$ mm and $\alpha \approx 3$ mrad. The radial intensity profile obtained from the inset diffraction pattern is plotted in pixel coordinates using the bottom and left axes (black curve), the red curve is the same data converted to real-space, normalized to its maximum value, and plotted using the top and right axes. The saturated portion of the detector signal was not included in the converted data.

A direct comparison between intensity distributions obtained from the ADF images and the pixelated STEM detector requires that the data are weighted similarly. Here, the distribution obtained with the pixelated detector has been modified to enable comparison on the same basis as the ADF image sets obtained using the aperture method. After subtracting a constant background (Fig. 9) from the radial intensity profile and multiplying the difference by $2\pi r dr$, where r is measured in pixels from the center of the pattern and $dr \approx 1$ pixel, the real-space intensity profile obtained from the inset diffraction pattern image is plotted in Fig. 9 (red curve) using the upper and right axes.

Comparing Fig. 3b and the real-space intensity profile of Fig. 9 demonstrates that the peak locations, their relative intensities, and the overall shapes obtained from ADF images and from the pixelated detector are in good agreement when plotted in the same coordinate space. Although the pixelated detector enables better angular resolution as suggested by the sharper peaks, a narrower aperture selected for a specific scattering range and smaller CL step size would enable better resolution for the ADF image method. The standard deviation curve normalized to $d\beta$ (Fig. 3b) may also offer some benefit to quantifying the peak positions and their relative intensities, because the exponentially decreasing background due to incoherent scattering is largely removed. For example, the (111) peak at 29 mrad and the (200) peak at 33 mrad are better resolved in the standard deviation curve than in the average intensity curve. Beyond resolution considerations, the peak intensities in either distribution of Fig. 3b can conceivably be used for texture analysis [15]. For example, when averaged over a large collection of grains, as was done here, the (220) peak shows greater intensity than the (111) peak suggesting non-random grain orientation.

Intensity distributions of the platinum sample obtained from ADF images (Fig. 8) change in complex ways with sample thickness. To verify that the observed results were not an artifact of the aperture system imaging method, Fig. 10 shows scattering intensity distributions (i.e., diffraction patterns) of the platinum pads obtained using the pixelated STEM detector. For these data, a 30 keV primary electron beam was focused at a spot on each pad for 10 s, and an image of the diffraction pattern was recorded with $CL \approx 13.2$ mm and $\alpha \approx 2.4$ mrad. Fig. 10a shows radial intensity profiles obtained from the diffraction patterns obtained with the pixelated detector, and an image of the diffraction pattern obtained from pad 2. Fig. 10b shows the data converted to real-space coordinates for direct comparison with Fig. 8b.

The platinum intensity distributions obtained from ADF transmission images, and diffraction patterns from the pixelated STEM detector are in good agreement. However, there are two notable differences. One

difference is that the ultrathin carbon substrate intensity is greater (relative to the platinum pads) in the distributions obtained with the pixelated detector than with the aperture system. This is because the electron beam was focused at a single spot for 10 s while recording the diffraction pattern with the pixelated detector. When scattering patterns are collected with the beam focused at a single spot, adventitious carbon can accumulate at the spot resulting in increased local sample thickness [16]. This additional thickness will alter the scattering intensity distribution and will be especially noticeable for ultrathin, low atomic number samples. Although a larger scan area could have been used to collect the diffraction patterns with the pixelated detector, the intention behind using a single spot was to demonstrate that one of the well-known SEM imaging artifacts can easily alter STEM-in-SEM image contrast. Two workarounds for this artifact include maintaining clean vacuum and low-dose imaging techniques. The other difference is that the distribution intensities fall more rapidly with increasing scattering angle in the pixelated detector data than in the aperture-based data. This is primarily due to detector efficiency differences, wherein the aperture data may better reflect the true scattering intensity distribution at larger angles.

It should not be surprising that ring-type electron diffraction patterns can be obtained from ADF image intensity measurements since each image essentially comprises a narrow annular slice of the electron scattering distribution. Experimentally, this is equivalent to conventional X-ray powder diffraction methods that scan through and measure intensities at different angles. It is unconventional, however, to obtain diffraction patterns from specific areas in a set of STEM-in-SEM images such as those recorded here. This approach is loosely related to the selected-area diffraction technique commonly used in conventional TEM [17]. One difference between the techniques is that the incident beam angle is slightly different for each raster spot in STEM-in-SEM images, meaning that the diffraction conditions change slightly, and that the diffraction pattern moves slightly as the beam is scanned across the sample. Another difference is that because focus is kept at the sample, the beam convergence angle, α , increases slightly (Fig. 1) as the sample is moved towards the pole piece. These differences should not significantly detract from the utility of the technique presented here if the average intensity of a sufficiently small region of interest is measured in an image, or an image is recorded at sufficiently high magnification. In the absence of a position- or angle-sensitive detector, the method described here can be used to quantify electron scattering behavior in specific regions of a sample and to assist with image interpretation as discussed in the next section. Samples appropriate for this technique include powders, amorphous samples, or others that exhibit ring-type scattering patterns. Scattering patterns from samples with large grains can also be quantified, but annular apertures will not enable spots, streaks, or lines to be discerned. Alternatively, apertures that enable spot diffraction patterns to be quantified in meaningful ways can be implemented in a straightforward manner [18]. Moreover, masks with annular apertures significantly narrower than any currently available annular solid-state detector, or apertures with complex non-conventional geometries can be easily fabricated in common household aluminum foil using a focused Ga^+ ion beam. A supporting structure for the foil mask can be made in a few minutes using an inexpensive 3D printer.

4.2. Image contrast

The electron-beam deposited amorphous carbon and amorphous platinum samples illustrate some of the challenges involved with interpreting contrast in ADF STEM-in-SEM images. Both samples exhibit contrast that changes from strong, to weak, to nonexistent depending on the imaging conditions and thickness. For ultrathin samples like the carbon pads, image intensities are anticipated to be proportional to the local mass-thickness provided that the mean free path for electron scattering in the material comprising the sample is greater than the

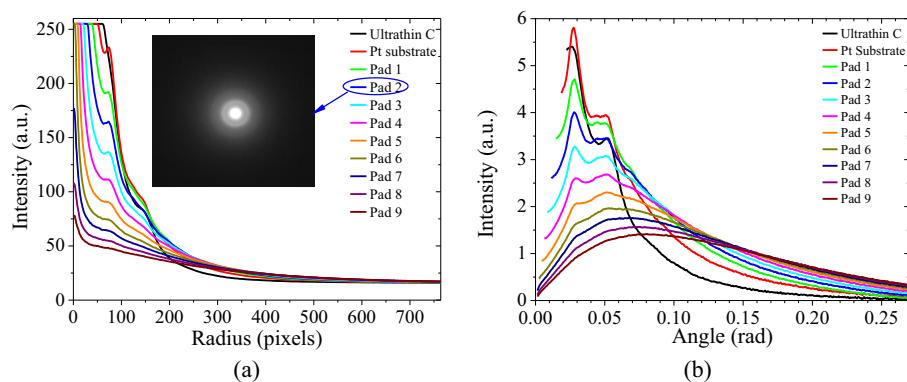


Fig. 10. Scattering intensity distributions of the platinum sample at 30 keV and $CL \approx 13.2$ mm. (a) Intensity profiles of scattering patterns recorded with the pixelated detector. The inset image shows a $1528 \text{ pixel} \times 1528 \text{ pixel}$ scattering pattern obtained from pad 2. (b) Intensity distributions in real-space coordinates. Scattering regions where the detector was saturated are not included.

sample thickness [19]. The total mean free path for electron scattering (elastic + inelastic) in carbon varies from approximately 4.4 nm at 10 keV, to 9 nm at 20 keV, to 14 nm at 30 keV [20]. Conservatively estimating the ultrathin carbon substrate at 5 nm thick (it is probably thinner), the maximum thickness of the carbon pad sample is approximately 14 nm, meaning that single scattering should be more likely than multiple scattering at 20 keV and 30 keV. In the dark-field, each incremental thickness increase should therefore elicit a proportional increase in signal intensity without significantly changing the shape of the scattering distribution [21]. Interpreting ADF image contrast for this carbon sample at 20 keV and 30 keV should be straightforward at the scattering angles employed here: the thickest region will exhibit the greatest intensity and strongest contrast with respect to the background vacuum intensity. Except at the smallest scattering angles, similar behavior is observed at 10 keV.

The platinum sample comprises a large range of thicknesses that are significantly greater than the total mean free path of 30 keV electrons in this material. As might be anticipated, the intensities do not change proportionally with thickness for a wide range of β_{mid} , and therefore ADF image contrast interpretation is not straightforward for a large range of acceptance angles. Indeed, it has long been established that no specific bright- and dark-field images exist for thick objects because the scattering intensity distributions tend to be broad and Gaussian-like [10,22]. This is demonstrated in Fig. 11a which shows the thickness-intensity relationship for the platinum sample at 30 keV. Considering a single curve in this figure, contrast can be interpreted as dark-field where the slope is positive, bright-field where the slope is negative. Contrast reversal occurs at inflection points, meaning that two different thicknesses can result in the same signal intensity.

One way to resolve the intensity-thickness ambiguity is to consult the diffraction patterns(s). For this platinum sample and the imaging conditions used here, the scattering distributions (Figs. 8b and 10b) indicate that thickness contrast interpretation is only straightforward when $\beta_{mid} < \sim 20$ mrad or $\beta_{mid} > \sim 200$ mrad. Image contrast between

those two acceptance angles will not necessarily reflect the sample thickness in an easily identifiable way. In some instances, it may be feasible to resolve the ambiguity by changing the accelerating voltage [23], which can elicit changes in the thickness-intensity curves (i.e., inflection points may move and/or slopes may change.) For example, consider the intensity-thickness relationship for the carbon sample at 10 keV (Fig. 11b) and 20 keV (Fig. 11c). The data shown there support previous reports stating that when the sample thickness is approximately equal to the mean free path, extreme care must be taken when interpreting images because contrast reversal can easily happen [24]. By using 20 keV primary electrons instead of 10 keV, the mean free path is greater than the thickness of most of the pads, the transition from bright- to dark-field character is avoided over the range of β examined here, and all images exhibit dark-field contrast. Moreover, for this ultrathin carbon sample a linear thickness-intensity relationship is observed, and sensitivity increases with decreasing acceptance angles. For the thicker platinum sample (Fig. 11a), a linear relationship between intensity and thickness is only observed at large acceptance angles. Decreasing the accelerating voltage will shift the maxima to the right and the scattering distributions will broaden.

The short-range order represented by the local maxima at $\beta_{mid} < 100$ mrad in Figs. 6 and 8 also presents potential hurdles for contrast interpretation. For example, consider the 30 keV carbon distributions of Fig. 6a. If nothing else were known about the sample, and only four images were recorded (i.e., at 15, 30, 60, and 90 mrad), one might assume based on scattering angle vs. intensity plots from *only* these four images that the scattering intensity distributions were approximately Gaussian shaped, and therefore that the sample was thicker than the AFM measurements indicated [9,22]. To avoid this potential source of confusion, and especially if sample thickness is unknown, several images should be recorded to evaluate the shape of the scattering distribution(s) over a large acceptance angle range, and to locate inflection and intersection points in the distributions. Note that these inflection points may not be detectable if an aperture with a wider acceptance

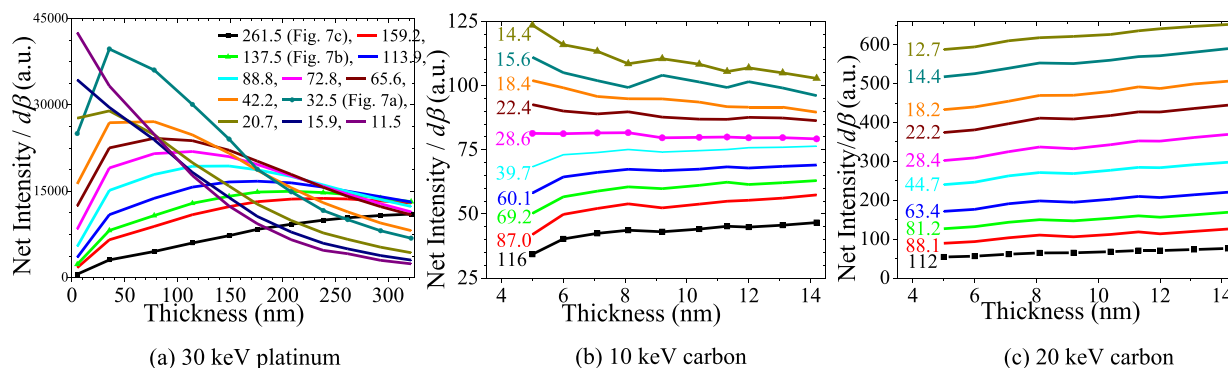


Fig. 11. The relationship between image intensity and sample thickness as a function of β_{mid} (mrad) for (a) the platinum sample at 30 keV, (b) the carbon sample at 10 keV, and (c) the carbon sample at 20 keV. Each line corresponds to intensities measured from a single image, and inset numbers indicate β_{mid} for the image.

angle span is used [14].

The samples examined here were not specifically selected to demonstrate atomic number contrast (i.e., *Z*-contrast). But, since *Z*-contrast is essentially a special case of mass-thickness contrast where coherent scattering does not largely contribute to the signal [8], that imaging mode is briefly addressed. According to one criterion [25], β_i should be greater than 160 mrad for 30 keV electrons in aluminum to largely disregard coherent scattering contributions in *Z*-contrast images. The absence of sharp, intense peaks in the distributions of Figs. 3 and 9 demonstrates that coherent scattering is indeed negligible at 160 mrad. No equivalent criterion exists for amorphous samples, and Monte Carlo electron scattering simulations, which are frequently employed to assist with image contrast interpretation, do not currently include provisions to account for any type of structural ordering. However, Monte Carlo based methods do adequately reproduce the general shape of the intensity-thickness distributions for the platinum sample, and can be useful for STEM-in-SEM image contrast interpretation.

If intuitive interpretation of mass-thickness contrast is desired, but knowledge of the scattering distribution and sample thickness is unavailable, a recommendation is to record both a bright-field and high-angle ADF image. Provided that the bright-field detector does not collect a significant fraction of electrons scattered out of the direct beam, these two images should be able to deliver a sense of the range of mass-thicknesses that exists in a sample.

5. Conclusion

Ring-type transmission electron diffraction patterns can be deduced from a set of ADF STEM-in-SEM images recorded with a basic solid-state detector and a narrow annular aperture. Those diffraction patterns can be used as an aid to interpret image contrast and for setting up imaging conditions. For the thick amorphous samples considered here, the large range of thicknesses resulted in electron scattering distributions indicating that image contrast is not necessarily intuitively interpretable over a wide range of acceptance angles. As with crystalline samples, if intuitive and quantitative contrast interpretation is desirable, thick amorphous samples should be imaged at large scattering angles where coherent scattering is negligible. Ultrathin samples, however, may be more amenable to quantitative imaging at smaller angles because intensity may be more sensitive to thickness, and greater accelerating voltages because the intensity-thickness relationship may be more linear.

Declaration of Competing Interest

The authors declare that they have no known competing financial

interests or personal relationships that could have appeared to influence the work reported in this paper.

References

- [1] R.R. Keller, R.H. Geiss, *J. Microsc.* 245 (2012) 245–251, <https://doi.org/10.1111/j.1365-2818.2011.03566.x>.
- [2] P.W. Trimby, *Ultramicroscopy* 120 (2012) 16–24, <https://doi.org/10.1016/j.ultramic.2012.06.004>.
- [3] C. Sun, E. Müller, M. Meffert, D. Gerthsen, *Adv. Struct. Chem. Imag.* 5 (2019) 1–9, <https://doi.org/10.1186/s40679-019-0065-1>.
- [4] G.H. Smith, R.E. Burge, *Proc. Phys. Soc.* 81 (1963) 612–632, <https://doi.org/10.1088/0370-1328/81/4/303>.
- [5] P.G. Merli, V. Morandi, F. Corticelli, *Ultramicroscopy* 94 (2003) 89–98, [https://doi.org/10.1016/S0304-3991\(02\)00217-6](https://doi.org/10.1016/S0304-3991(02)00217-6).
- [6] F. Grillon, *Microchimica Acta* 155 (2006) 157–161, <https://doi.org/10.1007/s00604-006-0535-8>.
- [7] Pfaff, et al., *J. Microsc.* 243 (2011) 31–39, <https://doi.org/10.1111/j.1365-2818.2010.03475.x>.
- [8] J. Holm, R.R. Keller, *Ultramicroscopy* 167 (2016) 43–56, <https://doi.org/10.1016/j.ultramic.2016.05.001>.
- [9] D.B. Williams, C.B. Carter, *Transmission Electron Microscopy*, 1st Ed. Plenum Press, New York, 1996.
- [10] H. Rose, J. Fertig, *Ultramicroscopy* 2 (1976) 77–87, [https://doi.org/10.1016/S0304-3991\(76\)90518-0](https://doi.org/10.1016/S0304-3991(76)90518-0).
- [11] U. Golla, B. Schindler, L. Reimer, *J. Microsc.* 173 (1994) 219–225, <https://doi.org/10.1111/j.1365-2818.1994.tb03444.x>.
- [12] V. Morandi, P.G. Merli, *J. Appl. Phys.* 101 (2007) 114917, <https://doi.org/10.1063/1.2745333>.
- [13] B. Caplins, J. Holm, R.R. Keller, *Ultramicroscopy* 196 (2019) 40–48, <https://doi.org/10.1016/j.ultramic.2018.09.006>.
- [14] J. Holm, *Ultramicroscopy* 195 (2018) 12–20, <https://doi.org/10.1016/j.ultramic.2018.06.007>.
- [15] J.L. Lábár, *Microsc. Microanal.* 14 (2008) 287–295, <https://doi.org/10.1017/S1431927608080380>.
- [16] M.T. Postek, A.E. Vladár, K.P. Purushotham, *Scanning* 36 (2014) 347–355, <https://doi.org/10.1002/sca.21124>.
- [17] J.B. Le Poole, *Phillips Tech. Rundsch.* 9 (1947) 93.
- [18] Caplins, B., Holm, J., Keller, R.R. *Carbon*, 149 (2019) 400–406. [10.1016/j.carbon.2019.04.042](https://doi.org/10.1016/j.carbon.2019.04.042).
- [19] L. Reimer, *Springer series in optical sciences vol 36, Transmission Electron Microscopy*, Springer-Verlag, Berlin, 1993 3rd Ed..
- [20] L. Reimer, *Springer series in optical sciences vol 45, Scanning Electron Microscopy*, Springer-Verlag, Berlin, 1985.
- [21] R.D. Heidenreich, *Fundamentals of Transmission Electron Microscopy*, Interscience Publishers, New York, 1964, p. 30 page.
- [22] D.J. Smith, J.M. Cowley, *Ultramicroscopy* 1 (1975) 127–136, [https://doi.org/10.1016/S0304-3991\(75\)80015-5](https://doi.org/10.1016/S0304-3991(75)80015-5).
- [23] T. Volkenandt, E. Müller, D. Gerthsen, *Microsc. Microanal.* 20 (2014) 111–123, <https://doi.org/10.1017/S1431927614002438>.
- [24] A.V. Crewe, T. Groves, *J. Appl. Phys.* 45 (1974) 3662–3672, <https://doi.org/10.1063/1.1663833>.
- [25] M.M.J. Treacy, J.M. Gibson, *Ultramicroscopy* 52 (1993) 31–53, [https://doi.org/10.1016/0304-3991\(93\)90020-X](https://doi.org/10.1016/0304-3991(93)90020-X).